

ENSO Evolution and Teleconnections in IPCC's 20th Century Climate Simulations: Realistic Representation?

Renu Joseph

Department of Atmospheric & Oceanic Science

and

Sumant Nigam

Department of Atmospheric & Oceanic Science, and
Earth System Science Interdisciplinary Center

University of Maryland, College Park, MD 20742-2425

(Submitted to the *Journal of Climate* on June 30, 2005; revised December 4)

Corresponding author: Sumant Nigam
3419 Computer & Space Sciences Bldg.
University of Maryland, College Park, MD 20742-2425
Email: nigam@atmos.umd.edu

Abstract

The study focuses on assessment of the spatio-temporal structure of ENSO variability *and* its winter climate teleconnections to North America in the IPCC AR4 simulations of 20th century climate. The 1950-1999 period simulations of six IPCC models [GFDL CM2.1, GISS-EH, CCSM3, PCM, HADCM3 and MIROC3.2 (hires)] are analyzed in an effort to bench-mark models in simulation of this leading mode of interannual variability.

The standard deviation of monthly SST anomalies is maximum in the Nino3 region in all six simulations, indicating progress in modeling of ocean-atmosphere variability. The broad success in modeling ENSO's SST-footprint – quite realistic in CCSM3 – is however tempered by the difficulties in modeling ENSO evolution: Biennial oscillation in CCSM3, and no regular warm-to-cold phase transition in the MIROC model. The spatio-temporal structure, including seasonal phase-locking, is on the whole, well modeled by HADCM3; but there is room for improvement, notably, in modeling the SST foot-print in the western Pacific.

ENSO precipitation anomalies over the tropical Pacific and links to North American winter precipitation are also realistic in the HADCM3 simulation; and, to an extent, in PCM. Hydroclimate teleconnections that lean on stationary component of the flow, such as surface air temperature links, are however not well modeled by HADCM3 since the midlatitude ridge in the ENSO response is incorrectly placed in the simulation; PCM fares better.

The analysis reveals that climate models are improving but still unable to simulate many features of ENSO variability *and* its circulation and hydroclimate teleconnections to North America. Predicting regional climate variability/change remains an onerous burden on models.

1. Introduction

The Intergovernmental Panel for Climate Change (IPCC) produces periodic assessment of our planet's future climate, specially, the change due to increasing greenhouse gases and aerosols. Assessments are made every five years, utilizing state-of-the-art climate system models and refined scenarios of changing landscape and atmospheric emissions, but projections continue to be undermined by caveats on model performance. The assessment process involves extensive analysis of model projections; and this year, a concerted program of model evaluation as well, to quantify the model deficiencies. The large number of models participating in the current round of IPCC assessment and the need to place projections of global and regional climate change in context created the US Climate Variability's (CLIVAR's) Climate Model Evaluation Project (CMEP; http://www.usclivar.org/CMEP_AO.html).

The focus on model evaluation necessarily lead to simulations, as opposed to projections or predictions; and on recent climate, for which validating observations exist. Climate system models (i.e., coupled atmosphere-ocean-landsurface-cryosphere models) participating in the current IPCC assessment (AR4) were asked to additionally simulate the climate of the 20th century using specified, time-dependent greenhouse gases, aerosol loadings and solar forcing. The bench-mark simulations were motivated, among others, by the belief that demonstration of models' potential in simulating seasonal climatologies and teleconnections manifest in present-day conditions would lend credence to model predictions of global and regional climate change.

Climate system models are evaluated here by examining the extent to which they simulate key features of the leading mode of interannual climate variability:¹ El Nino Southern Oscillation (ENSO). ENSO is a dominant pattern of ocean-atmosphere variability with substantial global climate impact; circulation and hydroclimate impacts are seasonally dependent but amplitudes are typically largest in boreal winter when ENSO SST anomalies are strongest. Devastating floods and droughts associated with ENSO events are the result of teleconnections between SST fluctuations

¹Models' potential in simulating seasonal variability is ascertained in an accompanying paper (Joseph and Nigam 2005).

in the tropical Pacific basin and near and distant regional climates (Ropelewski and Halpert 1987). The considerable societal impact of ENSO events (e.g., Chagnon 1999) and the possibility of global climate change being manifest in altered ENSO structure, duration and return-frequency places premium on realistic simulation of this variability mode. Modeling evidence for global climate change being ENSO-like is, however, not unequivocal.²

The present study focuses on assessment of the spatio-temporal structure of ENSO variability *and* its climate teleconnections in the IPCC AR4 simulations of 20th century climate. The assessment will reveal the models' potential in generating realistic interannual ocean-atmosphere variability in current climate conditions, and place model-based global and regional climate change projections in context. The assessment follows recent ENSO intercomparisons in CMIP control integrations (Achutarao and Sperber 2002) and the El Niño Simulation Intercomparison Project (ENSIP; Latif et al. 2001). The current analysis is however more atmospherically biased, given the focus on ENSO's circulation and hydroclimate teleconnections. The ocean component of ENSO variability is examined by van Oldenborgh et al. (2005), through intercomparisons of wind stress and thermocline depths in IPCC's 20th century climate simulations. These broader comparative studies have been supplemented by more in-depth analysis of ENSO variability in some simulations: GFDL (Wittenberg et al. 2005) and CCSM3 (Deser et al. 2005). Changes in ENSO variability in the global warming simulations, on the other hand, are examined by Collins et al. (2005) and van Oldenborgh et al.

The footprint of SST anomalies in ENSO's mature phase, monthly lead/lag autocorrelation of the ENSO index, preferred season for occurrence of the mature phase (phase locking), and SST evolution at the equator are analyzed in this study. The footprint, specially, the longitudinal location and extent of the sizeable tropical SST anomalies is important for the far-field response, through

²Some analyses attest to the similarity (e.g., Joseph et al. 2004; Boer et al. 2000; Timmermann et al. 1999; Meehl and Washington 1996), while others (e.g., Collins et al. 2005, van Oldenborgh et al. 2005) don't. Collins et al. examined climate change projections produced by the CMIP (Coupled Model Intercomparison Project) project, while van Oldenborgh et al. analyzed the current suite of IPCC AR4 model projections.

modulation of deep convection. Lead/lag autocorrelations, on the other hand, reflect important ENSO life-cycle properties (e.g., Trenberth and Stepaniak 2001; Torrence and Webster 1998; Thompson and Battisti 2001). The phase locking feature of ENSO (e.g., Rasmusson and Carpenter 1982; Trenberth 1997) imparts seasonality to the ENSO teleconnections; ENSIP integrations did not exhibit any seasonal preference (Latif et al. 2001) but some of the CMIP simulations (Achutarao and Sperber 2002) did.

ENSO teleconnections are of great interest from the climate impact perspective. Simulations of 20th century climate are thus analyzed for the veracity of ENSO teleconnections in circulation and hydroclimate. The teleconnections are strongest in boreal winter, coincident with the ENSO mature phase (e.g., Horel and Wallace 1981). ENSO circulation teleconnections reflect the dynamical link between tropical Pacific and the larger Pacific - North American region (and beyond). Circulation linkages are best expressed at an upper-tropospheric level where divergent outflow in the Tropics is manifest (e.g., Nigam 2003). Winter teleconnections greatly influence regional rainfall and temperature over the US west and Gulf coasts (e.g., Ropelewski and Halpert 1987; Trenberth et al. 1998; Kiladis and Diaz 1989; Nigam 2003) and the fidelity of their expression in 20th century climate simulations will be an important measure of the readiness of the IPCC AR4 models for making projections of *regional* climate change.

The IPCC simulations are also examined for representativeness of the zonally symmetric component of ENSO variability, which consists of warming of the Tropics and intensification of the thermally direct circulation: Modulation of the Hadley cell and its relation to subtropical jet anomalies. Intercomparison of ENSO's zonally-symmetric atmospheric component provides yet another measure of the efficacy of divergent-rotational flow interaction in the component atmospheric models.

The IPCC models and verification data sets are briefly described in section 2. Only six simulations are examined in this study, for reasons of resources. Besides the four US models (CCSM3, GFDL-CM2.1, PCM, and GISS-EH), one European (HADCM3) and one Japanese

(MIROC3.2) model was selected.³ The ENSO features are intercompared in section 3 while the climatological, seasonally-varying background states found important in determining ENSO evolution (Fedorov and Philander 1997; Kirtman and Schopf 1998) are intercompared in an accompanying paper that targets seasonal variability (Joseph and Nigam 2005).⁴ ENSO circulation and hydroclimate teleconnections are analyzed in section 4 while the zonally-symmetric component of ENSO's atmospheric response is intercompared in section 5. Concluding remarks follow in section 6.

2. Data Sets

The 20th century climate simulations analyzed in this study are obtained from the Program for Climate Model Diagnostics and Intercomparison (PCMDI) data archives. Twenty one climate system (coupled) models from various national and international modeling centers are participating in IPCC's 4th Assessment Report (AR4). Multiple simulations are obtained for the same period from each model, but only the first one (Run 1) is analyzed here. A single realization of 50 years duration may not be sufficient for characterization of ENSO variability, but the latter half of the 20th century is nonetheless chosen for analysis in the interest of overlap with validation data sets, which include global reanalyses.

Reported intercomparisons focus on six climate system models: Four from the United States: [NOAA/GFDL-CM2.1](#) (PCMDI 2005a); [NASA/GISS-EH](#) (PCMDI 2005b); [NCAR's CCSM3](#) (PCMDI 2005c); and [NCAR's PCM](#) (PCMDI 2005d). One from the United Kingdom, Hadley Centre's [HADCM3](#) (<http://www.met-office.gov.uk/research/hadleycentre/models/HadCM3.html>) and one from Japan, [MIROC3.2](#) (hires, PCMDI 2005e). Models differ in numerical representation schemes and

³Of the simulations exhibiting reasonable ENSO variability, only the ECHAM5/MPI-OM is not on this list (van Oldenborgh et al. 2005).

⁴Simulated SST and the divergent east-west circulation at the equator are intercompared in the season of maximum zonal SST-gradient (September-October). Models are unable to produce a robust SST cold-tongue in the eastern tropical Pacific; a modest cold bias is also evident at the equator in most models. Achutarao and Sperber (2002) and Latif et al. (2001) noted similar problems in earlier versions of these models.

resolution of the component atmosphere and ocean models. Important information on each of the six models can be found at the indicated web sites. Despite differences in numerical representation and physical parameterizations, the essential dynamics of the atmosphere and ocean should be similarly represented in the models. To facilitate intercomparison, simulation data sets were regrided to the Gaussian grid associated with spectral rhomboidal truncation at wave number 30; which is roughly equivalent to a $3.75^\circ \times 2.25^\circ$ longitude-latitude grid.

Several observationally constrained analyses are used in assessment of ENSO variability. These include the two global atmospheric reanalyses: NOAA's National Centers for Environmental Prediction (NCEP; <http://www.cdc.noaa.gov/cdc/data.ncep.reanalysis.html>; Kalnay et al.1996) and the European Centre for Medium Range Weather Forecasts (ECMWF; <http://www.ecmwf.int/products/data/archive/descriptions/e4/>; called ERA-40) data sets. The SST reference data set is the Hadley Center's sea-ice and SST analysis (the HadISST data; Rayner et al. 2003). Target fields are generated, whenever possible, from regressions in periods synchronous with the model output being evaluated. Regressions are computed from monthly data, mainly, in the boreal winter season, which is taken to be December-March in this paper.

3. ENSO SSTs

The structure and evolution of ENSO SST anomalies is obtained from regressions of the ENSO index. The index is based on the distribution of SST standard deviation (SD), which is computed from anomalies of all calendar months; and not just boreal winter, for there is no assurance that ENSO SST variability peaks in this season in the model simulations. Examination of the SD distributions (not shown) reveals that the Nino3 box (5°S - 5°N ; 150°W - 90°W) encompasses the SD maximum in the tropical Pacific in all cases; observations and model simulations. This, in itself, is remarkable progress in modeling of ocean-atmosphere variability. The Nino3 SST index – areally-averaged SST anomalies in the Nino3 box – is used as marker of ENSO variability and contemporaneous index-regressions are used to intercompare ENSO features and the associated

circulation and hydroclimate teleconnections.

SST structure

All-month SST regressions of the Nino3 SST index are shown in Fig. 1 for observations and simulations. The top panel (target) is obtained from regressions on HadISSTs, and the resulting pattern is a mix of both nascent and mature phase ENSO SST anomalies; given that regressions are computed using all-calendar-month data. Observed amplitudes are, not surprisingly, largest in the eastern equatorial Pacific; approaching 1.2K. The Nino3 index regressions in the simulations are broadly similar but for varying amplitudes and westward pattern-extent, and general confinement of SST anomalies to the equatorial latitudes. CCSM3 and PCM exhibit reasonable distributions except near the South American coast. HADCM3 and GFDL models stand out in context of westward pattern-extent; regressions remain significant up to the Maritime Continent in both cases; at variance with observations. The GFDL model is also too energetic along the equator, by a factor of 2, while the MIROC model is too weak; both are outliers. GISS model regressions are also weak and too tightly focused in the Nino3 region.

SST evolution

The ENSO life-cycle is analyzed in Fig. 2, through lead/lag autocorrelations of the Nino3 SST index. The autocorrelation statistic is a simple, straightforward way to analyze event-longevity and oscillatory behavior. All calendar months are used in computing autocorrelation which is lead/lag symmetric, about the maximum value of 1.0. The shape of the autocorrelation curve, in particular, its width at de-correlation values (e^{-1}) provides an estimate of event duration in any one phase; a horizontal line is drawn at $e^{-1} = 0.368$ to facilitate estimation. The width is about 13 months in case of observations and HADCM3 and GFDL simulations, but significantly smaller (~10 months) in CCSM3, GISS and PCM simulations; and considerably longer (~18 months) in the MIROC simulation.

The change in autocorrelation-sign reflects connectivity to the opposite phase of variability,

specially, if autocorrelation attains significant negative values. If the same threshold for significance (e^{-1}) is used, as before, only 2 simulations cross over: CCSM3 and, to an extent, GFDL. Excepting these two, climate system models exhibit little propensity to move from one phase of ENSO variability to the other on a regular basis; El Niño-to-La Niña (or vice-versa). The MIROC model, in fact, wants to keep the same phase over the analyzed interval (36 months); in variance with observations and all other models.

It is interesting that while both CCSM3 and GFDL attain significant negative values, they do so at different lead/lags: at 12 and 18 (or more) months, respectively. Large negative values of the autocorrelation at 12-month lag indicates oscillatory behavior at biennial time scales; the case in CCSM3, as shown in the next figure. The 36-month analysis window is, apparently, not wide enough to ascertain if the GFDL index autocorrelation attains more negative values than 0.4. In any case, the period, if there is indeed an oscillation, is ≥ 36 months.

SST evolution at the equator

The evolution of ENSO SST anomalies in the equatorial Pacific is shown in Fig. 3. The 5°S-5°N averaged SST lead/lag regressions of the Niño3 index are plotted over a 36-month interval; time markings have no unique correspondence with calendar months. The composited evolution of ENSO SSTs during the latter half of the 20th century is portrayed. The top three panels depict observed evolution: over the entire record in the left panel, and in pre- and post- climate-transition periods in the middle and right panels. ENSO evolution proceeded somewhat differently in these two periods, with SST anomalies developing from east-to-west in the earlier period (e.g., Wang 1995), as evident in the Fig. 3 displays. SST evolution in the model simulations is shown in the remaining six panels, from regressions over the entire record; as such, their target is the top-left panel. The portrayals differ in several respects, but all except the GFDL one, exhibit east-to-west development, similar to that seen in the pre-climate-transition period evolution. The GFDL model is notable in showing coherent west-to-east SST development, at least in the El Niño precursor phase.

The Hovmoeller displays provide other interesting information on SST evolution as well. The oscillatory nature and period can be readily ascertained from these plots: The HADCM3 model exhibits reasonably realistic SST evolution. PCM generates more realistic zonal SST-extent but also shorter ENSO durations. CCSM3 has realistic amplitudes but suffers because of the biennial nature of variability, which is now clearly manifest. ENSO variability in the GISS and MIROC models is, evidently, quite weak. In contrast, ENSO variability is much too strong in the GFDL model, which also exhibits an oscillatory tendency, albeit at longer time scales (~3.5 years). Differences in longitudinal extent of the ENSO SST anomalies were noted earlier (cf. Fig. 1): The zonal extent is about right in CCSM3, but larger in other models, with GFDL being extreme in this regard.

Seasonal phase-locking

Several studies beginning with Rasmusson and Carpenter (1982) have noted that El Nino development occurs during the boreal spring-to-winter seasons, with SST anomalies in the central/eastern tropical Pacific peaking in winter. This seasonal synchronization is referred as phase-locking of ENSO variability. Seasonal phase-locking can be easily assessed by plotting standard deviation of the ENSO SST index in each calendar month (e.g., Trenberth 1997; Latif et al. 2001). Since ENSO development involves both spatial expansion and growth of SST anomalies, choosing an index biased towards the mature phase of ENSO can be helpful in ascertaining seasonal preference. Phase-locking is analyzed here using the Nino3.4 index, which represents areally-averaged SST anomalies in a slightly westward displaced box (5°S-5°N;170°W-120°W); Nino3.4 is highly correlated with Nino3, at least in observations.

Figure 4 shows the extent of ENSO phase-locking in observations and simulations of the latter half of the 20th century climate. Observed ENSO variability peaks in boreal winter, as anticipated, but model simulations exhibit varied behavior. HADCM3 and CCSM3 are apparently close to the observed distribution, while PCM stands out in view of its preference for both boreal

winter and summer.⁵ ENSO variability in the GFDL model, on the other hand, is not seasonally discriminating; note, the SD in this case is scaled down by a factor of 2, for plotting convenience. Variability in the GISS and MIROC models is weak, as noted before; and not significantly discriminating with respect to seasons.

4. ENSO teleconnections

Generating realistic ENSO variability remains challenging for climate models as evident from the preceding analysis of ENSO amplitude, duration, recurrence, and seasonal timing. Modeling ENSO's influence – climate teleconnections to near and far regions of the globe – is no less challenging, as discussed in this two-part section. The first is focused on the global Tropics and the Northern hemisphere, while the second targets hydroclimate impacts on North America. ENSO teleconnections are by no means confined to the winter season, although only these are examined below, in the interest of space.⁶ The teleconnections are obtained from monthly regressions of the Nino3 SST index during boreal winter (December-March).

Tropical precipitation

Key elements that generate ENSO circulation teleconnections are examined first: Tropical rainfall anomalies which release latent heat in the mid-troposphere and generate geopotential fluctuations that carry the ENSO signal to remote regions are shown in Fig. 5. The vertical distribution of heating anomalies is important for the remote response, but 3D diabatic heating is not

⁵CCSM3 too exhibits preference for these two seasons when the Nino3 index is used to mark ENSO variability. This preference is also evident in CCSM3's multi-century control integrations with present-day CO₂ concentration (Deser et al. 2005).

⁶ENSO teleconnections in the shoulder seasons (boreal fall and spring) are available at http://www.atmos.umd.edu/~nigam/renu/main_frame.htm. Although computed using anomalies from all years, the Fall (Spring) pattern can be safely interpreted as characterizing anomalies in the season preceding (succeeding) the ENSO mature-phase; ascertained from 3-month lead/lag regressions of the Nino3 DJF index. Interpretation of Nino3's contemporaneous summer regressions is however problematic in view of significant contributions from both pre- and post-ENSO summer anomalies; which are temporally equidistant from the ENSO mature-phase. As such, the 6-month lead (preceding summer) and lag (succeeding summer) regressions of the Nino3 DJF index are shown separately at the website. Also shown are teleconnections in the classically defined winter season (DJF) so that impact of including March in the Figures 5-8 winter regressions can be assessed.

archived in most of the IPCC simulations. As such, ENSO precipitation anomalies which represent the vertically averaged component of latent heating are intercompared here, along with vertical velocities in the core ENSO rainfall region (180-150°W, 7.5°S-5°N; marked in the ERA-40 rainfall panel in figure 5). The latter closely follow the vertical distribution of diabatic heating in the deep Tropics, as the dominant thermodynamic balance there is between $-N^2\omega$ and Q , where N^2 is the static stability, ω the pressure vertical velocity, and Q the diabatic heating rate.

Simulation targets are obtained from both NCEP and ERA-40 reanalyses in view of the sensitivity of tropical convection schemes, and given the widespread use of these data sets in model validation. It must be noted, though, that precipitation in the reanalyses is produced from forecasts (6-hour ones in NCEP), and as such, its consistency with the initiating reanalysis circulation is not assured. Precipitation in global reanalyses is, moreover, not directly constrained by observations – as are temperature and circulation – which leaves it susceptible to influences of physical parameterizations.

Satellite estimates of ENSO precipitation (Xie and Arkin 1997) would be a better reference for simulations, except that the satellite record is not long enough for development of robust composites. The satellite and reanalysis based ENSO precipitation anomalies were intercompared in the shorter, but ENSO-active, 1979-93 period by Nigam et al. (2000). Figure 6 of that paper shows the satellite anomaly to be different; specially, from NCEP's which is too weak and differently distributed, much as in Fig. 5 here. The ECMWF anomaly shown in that figure is from an earlier version of ERA-40 (ERA-15; <http://www.ecmwf.int/research/era/ERA-15>). The satellite anomaly depicts a largely zonal (or Walker-like) redistribution of tropical rainfall during ENSO; meridional redistribution is comparatively modest and focused mostly in the South Pacific Convergence Zone. The ERA-15 anomaly was similar to the satellite one, except for weaker suppression of precipitation over the Maritime Continent. NCEP anomaly, on the other hand, exhibited a more meridional (or Hadley-like) redistribution of rainfall.

The ERA-40 precipitation anomaly (Fig. 5) is very similar to the ERA-15 one discussed

earlier, and thus the target for model simulations in this analysis. ENSO precipitation anomalies in the GFDL model are too large; specially, rainfall reduction off the equator, which is a factor of 2 stronger than in ERA-40. In comparison, rainfall enhancement in the central equatorial Pacific is only 25% stronger, despite ENSO SST anomalies being twice as large in this model (cf. Fig. 1 and 3). Rainfall suppression over the Amazon is also much too strong. The GISS model, in contrast, produces a very weak ENSO signal in Pacific precipitation. ENSO SSTs are weak in the GISS model but even weaker in the MIROC model (cf. Fig. 1). Yet, the latter produces a more significant precipitation response; attesting to the importance of SST anomaly location. In view of the climatological east-west SST-gradient, a weaker but westward placed anomaly can meet the SST-threshold conditions for deep convection (Graham and Barnett 1987).

ENSO precipitation has realistic amplitude in the NCAR models but the anomalies are too confined, meridionally; too Hadley-like, specially CCSM3's. Rainfall enhancement in the eastern Pacific is to the south of the equator in both models, at variance with ERA-40 structure. Despite some deficiencies, notably in the eastern Pacific, precipitation anomalies in the HADCM3 model are, perhaps, more realistic than any; considering amplitude, rainfall suppression over South America, and the more Walker-like distribution.

Diabatic (latent) heating anomalies plays an important role in generating ENSO's local and remote influences. But as with heating's horizontal distribution, its vertical structure is accessible, only indirectly from the IPCC data archives; through vertical velocity; a good proxy in the deep Tropics, for reasons stated earlier. The vertical velocity ($-\omega$) profiles in the core rainfall region are computed from Nino3 regressions, and shown in Fig. 6.⁷ The extent of differences in the ω -profiles is striking: both between reanalyses and amongst models. GFDL has the strongest amplitude, in accord with the line-up of precipitation anomalies in the region. The CCSM3 profile is, perhaps,

⁷The ERA-15 and NCEP reanalysis based ENSO heating profiles in the same core rainfall region are shown in Nigam et al. (2000; their figure 10).

closest to ERA-40 (the assumed target) in overall structure, including vertical integral;⁸ except for the modest, but potentially consequential, slope difference in the lower troposphere (1000-850 hPa). The steeper slope reflects the somewhat “bottom-heavy” structure of CCSM3's ω -profile vis-a-vis ERA-40's; and reminiscent of key heating profile differences in ENSO observations and simulations (Nigam et al. 2000). Interestingly, the HADCM3 profile is nearly indistinguishable from ERA-40 in the lower troposphere. Different slopes (or $\partial\omega/\partial p$) reflect horizontal-convergence differences, in view of the continuity equation ($\partial\omega/\partial p = -\nabla_h \cdot \vec{v}$). The ENSO-related surface (1000 hPa) convergence over the central equatorial Pacific (not shown) is, accordingly, strongest in GFDL, and then CCSM3, ERA-40, HADCM3, and PCM simulations. The convergence arises mostly from the anomalous equatorward flow in both hemispheres in nature, i.e., from $\partial v/\partial y$ rather than $\partial u/\partial x$, as noted before (Rasmusson and Carpenter 1982, Deser and Wallace 1990, Nigam and Shen 1993, among others). The divergent flow differences are, of course, consequential for the structure of related zonal surface-wind differences; and ensuing ocean-atmosphere variability.

Extratropical circulation

ENSO's far-field circulation response cannot all be attributed to latent heating and cooling anomalies in the tropical Pacific, as it is shaped along the way by interactions with the Pacific stormtrack system and North American orography; see DeWeaver and Nigam (2004) for more discussion and references. Circulation teleconnections may thus exhibit limited sensitivity to the tropical latent heating and cooling structure.

ENSO teleconnections in 250 hPa geopotential heights are displayed in the right panels of Fig. 5. Teleconnection patterns obtained from NCEP and ERA-40 reanalysis – the model targets – are displayed in the top two panels; the patterns are nearly identical. ENSO height anomalies consist of a coherent four-cell pattern, extending from the tropical Pacific to the North American continent; with extensions into western Europe. Anomalies are strongest in the upper troposphere, as noted before; but modest (20-40 gpm), nonetheless. The pattern's tropical features are not discernible at

⁸The vertical integral of vertical velocity is proportional to local rainfall in the deep Tropics.

500 hPa, though; a pressure-level of choice in earlier teleconnection analyses (e.g., Wallace and Gutzler 1981). For these and other reasons, discrimination of ENSO teleconnection from other Pacific basin patterns – PNA (Pacific / North American) and the Western Pacific pattern – has proved challenging; see Nigam (2003) for an in-depth discussion.

The ENSO height response is characterized by the position of its features: subtropical ridge in the Pacific is centered southeastward of Hawaiian islands; trough in the North Pacific is centered in the Gulf of Alaska; the ridge over North America is positioned between the Great Lakes and Hudson Bay; and the trough to its south extends across the US southern tier states.

The ENSO teleconnection is reasonably modeled in the GFDL simulation, except for the ridge position, which is $\sim 30^\circ$ upstream, i.e., over the Pacific Northwest. The amplitude is larger by a factor of 2; in line with the correspondingly larger ENSO SST and rainfall amplitudes. ENSO height anomalies, in contrast, are exceedingly small in the GISS model; consistent with near-zero precipitation anomalies in the Pacific. Height anomalies in the two NCAR simulations are broadly similar except for different ridge locations over North America. Interestingly, the tropical ridge in both NCAR patterns is too weak; both in an absolute sense and relative to the amplitude of extratropical features; the PCM pattern is, overall, somewhat more realistic.⁹ The HADCM3 teleconnection suffers from the reverse error: a muted extratropical response; features are also incorrectly placed. The MIROC model produces an insignificant height response everywhere; not surprising, given the rather weak and unrealistic representation of ENSO variability in its simulation.

In summary, ENSO height anomalies have fairly realistic structure over the Pacific basin in four of the six simulations: GFDL, CCSM3, PCM, and HADCM3; specially, PCM. The near-field response arises from large-scale modulation of the regional Hadley and Walker circulations, and its robustness is noteworthy given the variations in distribution of modeled ENSO precipitation (and, possibly, latent heating and cooling in the vertical). The simulation of midlatitude ridges in the ENSO response however proves challenging for these very models: The North American ridge is produced

⁹Height anomalies in the NCAR models are broadly similar despite large differences in upper-level $\partial\omega/\partial p$ (Fig. 6); reflecting insensitivity of ENSO teleconnections to aspects of the equatorial Pacific heating distribution.

in all simulations but not always at the correct location; while the comparable amplitude ridge over western Europe is not captured in most simulations. Unlike the near-field response, the far-field component of ENSO teleconnection is generated from several processes, including interaction with the Pacific stormtrack system and North American orography; its inadequate portrayal reflects the incomplete representation of these interactions in model simulations.

North American hydroclimate

ENSO's influence on upper-tropospheric circulation is of interest from the viewpoint of teleconnection mechanisms, but its hydroclimate influence is of great societal importance. Hydroclimate refers to the near-surface climate elements that impact societal sustenance: precipitation, surface air temperature, soil moisture, and streamflow, for example. ENSO's influence on the first two of these fields is examined in this study.

Continental precipitation

The impact on North American precipitation in NCEP and ERA-40 reanalysis data sets is shown in Fig. 7; polar plots and a lower contour interval help reveal features not discernable in the earlier plot. The two precipitation anomalies are remarkably similar over North America despite phenomenal amplitude differences in the Tropics (cf. Fig. 5). Winters in central California and southeastern United States are wetter in El Nino years in both data sets, by as much 0.4 mm/day. The impact on California is more substantial since climatological rainfall rates there are smaller by 1-2 mm/day. The ENSO precipitation distribution reflects the influence of the geopotential anomaly pattern whose phase in the lower troposphere is similar to that at upper levels; the far-field height response is equivalent barotropic. Precipitation is thus higher where heights are lower; except in vicinity of orography, where forced ascent of low-level flow determines the rainfall regions.¹⁰

ENSO precipitation in the GFDL model favors the southeast. Larger than observed

¹⁰The rainfall pattern has also been ascribed to the southward shift of stormtracks over North America in El Nino winters. Height anomalies (cf. Fig. 5) do indicate the jet to be southwardly displaced. But the absence of a meridional dipole in continental precipitation suggests that this view is not supported by global reanalyses; or else integrity issues with reanalysis precipitation.

precipitation anomalies were expected over North America since SST and height anomalies in this simulation are too strong, by a factor of 2; but modeled anomalies are larger than reanalysis ones only over the southeastern US. Precipitation is reduced over the Pacific Northwest in the model during El Nino winters, leading to a meridional dipole along the US west coast; a feature, not found in reanalysis precipitation but present in station precipitation data (e.g., Green et al. 1997; Nigam 2003). CCSM3's precipitation response is apparently more problematic: Precipitation is enhanced in the Pacific Northwest and northern coastal California, and only marginally, along the eastern seaboard and Gulf coast. The PCM's response over land is more reasonable in comparison; in both amplitude and structure. ENSO precipitation anomalies in HADCM3 are more zonally oriented, and a close inspection of the location of positive anomalies and onshore flow over the west coast suggests that stormtrack changes are the cause of precipitation anomalies, i.e., transient rather than stationary moisture fluxes; presence of meridional dipoles at both coasts supports this assessment. Note, rainfall reduction over the Pacific Northwest – part of the west coast dipole – is realistically captured in the HADCM3 simulation.

Surface air temperature

Winter anomalies in surface air temperature (SAT) result mostly from changes in thermal advection; specifically, of climatological temperature by anomalous low-level winds, i.e., $-\mathbf{V}_a \cdot \nabla T_c$ where \mathbf{V}_a is the vector wind anomaly and T_c the climatological temperature. The equivalent barotropic structure of ENSO height anomalies over North America leads to southeasterly flow over the western/central continent, poleward of $\sim 30^\circ\text{N}$ in both global reanalyses. Not surprisingly, much of Canada and the Pacific Northwest, including Alaska, are warmer during ENSO winters; by up to 1K. Note, eastern Canada is warmer in spite of northeasterly flow since maritime rather than continental air is fluxed in. Global reanalyses are in accord in depicting a warmer (cooler) northern (southern) continent during El Nino winters.

SAT anomalies in the GFDL simulation are much stronger, in line with the overly strong ENSO SST, precipitation, and circulation anomalies (cf. Figs. 1 & 5). Consistent with the westward,

but erroneous, position of the North American ridge (Fig. 5) in the GFDL height response, the warming is focused westward – over Alaska – where SAT increases by ~2K. The PCM's SAT response is similar to GFDL's as the ridge is located westward of its observed position here too, but the response amplitude is much more reasonable. SAT response in the CCSM3 simulation also has realistic amplitudes but exhibits a pronounced southwest-to-northeast tilt, in variance with observed structure (Fig. 7, top-two panels), where the tilt is, if anything, in the other direction. The spurious orientation of CCSM3's SAT anomalies, of course, reflects the wedge-like shape and southwest-to-northeast tilt of the overlying North American ridge, which exerts a controlling influence on anomalous thermal advection. The shortcomings in HADCM3's simulation of ENSO's circulation response over North America are reflected in its SAT response, given the importance of anomalous flow in the generation of SAT anomalies; but, interestingly, not in its precipitation response. The two key elements of the hydroclimate response are, apparently, shaped by different components of the anomalous circulation in this model: precipitation, by the sub-monthly transients (or stormtrack fluctuations); while surface air temperature is impacted more by the stationary (monthly-mean) component of the flow. The robustness of this conclusion remains to be ascertained, though.

5. ENSO's zonally symmetric response

The zonally symmetric component of ENSO's response, which consists of warming of the Tropics and intensification of the thermally direct circulation, is intercompared in Fig. 8. The rotational (zonal-mean zonal wind) and divergent (zonal-mean meridional and vertical motions) anomalies in boreal winter are shown; NCEP and ERA-40 ones are in the top panels. The strengthening of the jet in El Nino winters has been noted in several studies (Bjerknes 1966; Arkin 1982; Nigam 1990; Hoerling et al. 1995; DeWeaver and Nigam 2000). The rotational response in Northern latitudes is similar, with the subtropical jet enhanced along its equatorward flank in both data sets; by ~3 m/s at the tropopause level; the ERA-40 response is marginally stronger. The symmetry of the rotational response (about the equator) must be related to the symmetrical structure

of accompanying divergent circulations: But the anomalous Hadley circulation is quite different in the two data sets, with ERA-40 having a cell in each of the hemispheres and NCEP having just one; in the Northern hemisphere. The discrepancy is disconcerting since NCEP does have a sizeable rotational response in the Southern subtropics; how is it produced? Such discrepancies can arise in context of reanalysis data sets where rotational flow is constrained by observations. The divergent component is not similarly constrained, and thus more influenced by the assimilating model's physical parameterizations.

Relationship of divergent and rotational flows shows interesting variations even within the same data set: the hemispheric variation in ERA-40's response, for example. The core of the jet anomaly is located at the terminus of the anomalous Hadley cell in the southern upper-troposphere, but not in the northern one. The northern cell terminates $\sim 10^\circ\text{N}$, but the jet-core is located much farther ($\sim 25^\circ\text{N}$). The early termination of the northern cell is a robust feature, being present in the NCEP anomalies (cf. Fig. 8), and also in the station-data based ENSO composites of Oort and Yienger (1996; figure 8). The reasons for non-collocation of the jet-core and divergent cell's terminus in ENSO's northern winter response remain to be investigated, but a southward shift of stormtracks and the related shift of the thermally-indirect Ferrel cell appear to be key. For example, if the shift was substantial – as over the Pacific during El Niño winters – the anomalous Ferrel cell can offset portions of the thermally-direct circulation anomaly; leading to a Hadley cell narrower than what would be obtained without stormtrack perturbation; and thus non-collocation.¹¹

The GFDL model's zonally symmetric response in El Niño winters is quite reasonable, except for the amplitude which is a factor of two too large. The position and symmetry of the jet anomalies and the width of the anomalous thermally direct cells are all quite realistic. The NCAR models have reasonable amplitude but the response is biased towards the Northern hemisphere. The relationship of rotational and divergent circulation anomalies is evidently distorted in the PCM model. The

¹¹The collocation of features in the Southern hemisphere supports the hypothesis involving stormtrack perturbations since ENSO-related jet anomalies do not have the reach to impact southern stormtracks which are located in the high midlatitudes ($\sim 50^\circ\text{S}$) in their summer season. ENSO induced thermally-direct circulation cannot thus be offset in the Southern subtropics; leading to collocation.

zonally-symmetric ENSO response is, perhaps, most realistic in the HADCM3 simulation. Except for some northern hemisphere bias, most other features are captured, including the weak tropical easterlies. The GISS and MIROC models are apparently unresponsive in the zonally-symmetric circulation component as well.

6. Concluding remarks

The study has focused on evaluation of climate system models participating in the IPCC assessment (AR4) of our planet's future climate. Projections of climate change, specially, on regional-to-continental scales, have often been undermined by the inadequate and/or incomplete representation of physical processes in climate system models. Model deficiencies are however less apparent if the focus is on the global-mean response; and that too in surface air temperature, as customary. Focusing on the global-mean surface temperature effectively precludes the atmospheric general circulation (and its errors) from impacting the outcome, which then depends more on the accuracy of radiative physics and transfer schemes; i.e., on modeling of energy balance; a simplification. Recent societal interest in hydroclimate variability and change has however lead to well-posed questions on regional-to-continental scale footprints of global change, leading to scrutiny of model projections on these scales.

The study seeks to evaluate the performance of climate system models in simulating key aspects of the leading basin-to-planetary scale mode of interannual climate variability: El Nino Southern Oscillation. The considerable societal impact of ENSO events and the possibility of global climate change being manifest in altered ENSO structure, duration, and return-frequency places premium on realistic simulation of this variability mode.

The present analysis is somewhat atmospherically biased given our interests, specially, in assessing the quality of ENSO teleconnections to North American hydroclimate. Besides, the ocean (subsurface) component of ENSO variability is examined in van Oldenborgh et al.'s (2005) analysis of wind stress and thermocline depth variations in the same set of 20th century climate simulations.

The main findings are:

- *ENSO's SST footprint*: Most realistic in CCSM3, with PCM and HADCM3 following; GFDL's is stronger by a factor of 2 and extends well into the western basin; MIROC's, on the other hand, is weaker by a factor of 2; GISS's is too tightly confined to the Nino3 region.

- *ENSO evolution*: Biennial oscillation in CCSM3; most realistic life-cycle in HADCM3; GFDL's life-cycle is a bit longer, along with a somewhat greater oscillatory tendency; MIROC does not exhibit regular warm-to-cold phase transitions.

ENSO SST anomalies at the equator exhibit east-to-west development in all models, except GFDL's, where SSTs develop the other way, much as in the post-climate-transition period.

- *ENSO phase-locking*: Nino3.4 SST index has largest amplitude in boreal winter in the HADCM3 and CCSM3 simulations, in accord with observations; GFDL model is not seasonally discriminating, while PCM's ENSOs favor both winter and summer, almost equally.

In summary, HADCM3 produces the most realistic ENSO variability among six models. Examination of the SST-anomaly distribution left three models in play: CCSM3, PCM, and HADCM3. The biennial nature of CCSM3's variability reduced the number of viable models to two, while the absence of seasonal phase-locking lead, by elimination, to HADCM3 being deemed most realistic from perspective of ENSO variability. Examination of additional models, variability modes (including seasonal-cycle), and other ENSO features can, of course, alter this conclusion.

- *ENSO's tropical precipitation*: HADCM3 anomalies are most like ERA-40's among the six models. NCAR model anomalies have realistic amplitude but are too confined, meridionally, and too Hadley-like; specially, CCSM3's. GFDL's anomalies are too large, specially, the rainfall reduction off the equator.

- *ENSO's circulation teleconnection*: Upper-troposphere height anomalies have fairly realistic structure over the Pacific in GFDL, CCSM3, PCM, and HADCM3; specially, in PCM. Robustness of the near-field response is noteworthy given the variations in distribution of tropical precipitation.

Simulation of midlatitude ridges in the ENSO response is however challenging for these models: The North American ridge is produced in all four cases but not at its observed position; it is located ~30°

upstream – over the Pacific Northwest – in most cases.

- *ENSO teleconnection to North American hydroclimate*: Wetter El Nino winters over central California and southeastern US (including Gulf Coast) are best modeled in the PCM and HADCM3 simulations. Location of circulation anomalies along the US west coast suggests that the teleconnection is grounded in stormtrack-shifts in HADCM3 but stationary moisture fluxes in PCM. GFDL produces a reasonable teleconnection along the west coast, but the response over Mexico and the southeast is much too strong. CCSM3's impacts are confined to more northern latitudes along both coasts.

ENSO teleconnections to surface air temperature, arising mostly from changes in thermal advection, are broadly realistic in the NCAR models; Canadian warming and continental cooling to the south are not correctly focused, though. Position of the North American ridge in ENSO's circulation response is, apparently, critical for the surface temperature impact. Not surprisingly, HADCM3 is unable to generate the ENSO related Canadian warming.

- *ENSO's zonally-symmetric response*: Model target here is the ERA-40 structure, where anomalous Hadley circulation comprises of a cell in each hemisphere; with the northern one being narrow (~10° wide). The subtropical jet anomalies are located ~25° away from the equator in both cases, though. HADCM3 produces reasonably realistic divergent and rotational anomalies. The NCAR models are biased towards the Northern hemisphere in rotational, but not divergent, anomalies; interestingly, PCM produces a stronger Hadley cell anomaly in the southern subtropics. GFDL has the right structure but excessive amplitudes; larger by a factor of 2.

The study suggests that climate system models are not quite ready for making projections of regional-to-continental scale hydroclimate variability and change, even though they have begun to make inroads in simulating key features of ENSO variability. Other modes of climate variability, including seasonal-cycle and intraseasonal variability, will all need to be analyzed. Assessments reveal model strengths and weaknesses and provide a context for interpreting model predictions of regional climate variability and change. Dynamically (or thermodynamically) oriented assessments can also produce credible hypotheses for model deficiencies, but do not, typically, provide

immediate recipes for improving the model's physics.

Acknowledgments

We greatly appreciate the feedback and guidance provided by Clara Deser, editor. We thank the reviewers for their helpful comments that lead to manuscript improvements.

The analysis was supported by US CLIVAR's Coupled Model Evaluation Project, through NSF Grant ATM0445134. Additional support was provided by DOE's Climate Change Prediction Program Grant DEFG 0201ER63258. Renu Joseph also acknowledges support via a subcontract from NSF Grant ATM0434221 (to Columbia University). Computational support for the project was provided by the National Computational Science Alliance via Grant ATM040008N for use of NCSA IBM P690.

We acknowledge the international modeling groups for providing their data for analysis, the Program for Climate Model Diagnosis and Intercomparison (PCMDI) for collecting and archiving the model data, the JSC/CLIVAR Working Group on Coupled Modeling (WGCM) and their Coupled Model Intercomparison Project (CMIP) and Climate Simulation Panel for organizing the model data analysis activity, and the IPCC WG1 TSU for technical support. The IPCC Data Archive at Lawrence Livermore National Laboratory is supported by the Office of Science, U.S. Department of Energy.

References

- Achutarao, K., and K. R. Sperber, 2002: Simulation of the El Niño southern oscillation: Results from the coupled model Intercomparison project. *Climate Dyn.*, **19**, 191-209.
- Arkin, P. A., 1982: The relationship between interannual variability in the 200mb tropical wind field and the Southern Oscillation. *Mon. Wea. Rev.*, **110**, 1393-1404.
- Bjerknes, J., 1966: A possible response of the atmospheric Hadley circulation to equatorial anomalies of ocean temperature. *Tellus*, **18**, 820-829.
- Boer, G.J., G. Flato, and D. Ramsden, 2000: A transient climate change simulation with greenhouse gas and aerosol forcing: projected climate for the 21st century. *Climate Dyn.*, **16**, 427-450.
- Chagnon, S. A., 1999: Impacts of 1997-98 El Niño-generated weather in the United States. *Bull. Amer. Meteor. Soc.*, **80**, 1819-1827.
- Collins, M., and coauthors, 2005: El Niño or La Niña like climate change? *Climate Dyn.*, **24**, 89-104.
- Deser, C., and J. M. Wallace, 1990: Large-scale atmospheric circulation features of warm and cold episodes in the tropical Pacific. *J. Climate*, **3**, 1254-1281.
- Deser, C., A. Capotondi, R. Saravanan, and A. Phillips, 2005: Tropical Pacific and Atlantic climate variability in CCSM3. *J. Climate* (in press).
- DeWeaver, E., and S. Nigam, 2000: Do stationary waves drive the zonal-mean jet anomalies of the northern winter? *J. Climate*, **13**, 2160-2175.
- DeWeaver, E., and S. Nigam, 2004: On the forcing of ENSO teleconnections by anomalous heating and cooling. *J. Climate*, **17**, 3225–3235.
- Fedrov A. V., and S. G. Philander, 1997: Is El Niño changing? *Science*, **288**, 1997-2002.
- Green, P. M., D. M. Legler, C. J. Miranda V, and J. J. O'Brien, 1997: The North American climate patterns associated with the El Niño–Southern Oscillation. COAPS Project Rep. Series 97-1, 8 pp. [Available online at [http://www.coaps.fsu.edu/lib/booklet/.](http://www.coaps.fsu.edu/lib/booklet/)]
- Graham, N.E., and T. P. Barnett, 1987: Sea Surface Temperature, Surface Wind Divergence, and Convection over Tropical Oceans. *Science*, **238**, 657-659.
- Hoerling, M. P., M. Ting, and A. Kumar, 1995: Zonal flow–stationary wave relationship during El Niño: Implications for seasonal forecasting. *J. Climate*, **8**, 1838–1852.
- Horel J. D., and J. M. Wallace, 1981: Planetary-scale atmospheric phenomena associated with the Southern Oscillation. *Mon. Wea. Rev.*, **109**, 813-829.
- Joseph, R., M. Ting, and P. J. Kushner, 2004: The global stationary wave response to climate change in a coupled GCM. *J. Climate*, **17**, 540-555.
- Joseph, R., and S. Nigam, 2005: IPCC 20th Century Climate Simulations: Intercomparison of

seasonal Circulation. (To be submitted to J. Climate)

Kalnay E., and coauthors, 1996: The NCEP/NCAR reanalysis project. *Bull. Amer. Meteor. Soc.*, **77**, 437-471.

Kiladis G.N., and H.F. Diaz, 1989: Global climatic anomalies associated with extremes in the Southern Oscillation. *J. Climate*, **2**, 1069-1090.

Kirtman, B. P., and P. S. Schopf, 1998: Decadal variability in ENSO predictability and prediction. *J. Climate*, **11**, 2804-2822.

Latif M., and coauthors (2001): ENSIP: The El Niño simulation Intercomparison project. *Climate Dyn.*, **18**, 255-272.

Meehl, G.A. and W.M. Washington, 1996: El Niño-like climate change in a model with increased atmospheric CO₂-concentrations. *Nature*, **382**, 56-60.

Nigam, S., 2003: Teleconnections. *Encyclopedia of Atmospheric Sciences*; Editors: J.R. Holton, J. A. Pyle & J. A. Curry; Academic Press, Elsevier Science, London, 2243-2269.

Nigam, S., C. Chung, E. DeWeaver, 2000: ENSO diabatic heating in ECMWF and NCEP–NCAR Reanalyses, and NCAR CCM3 simulation. *J. Climate*, **13**, 3152–3171.

Nigam, S., and H.-S. Shen, 1993: Structure of oceanic and atmospheric low-frequency variability over the Tropical Pacific and Indian Oceans. Part-I: COADS Observations. *J. Climate*, **6**, 657-676.

Nigam, S. 1990: On the structure of variability of the observed tropospheric and stratospheric zonal-mean zonal wind. *J. Atmos. Sci.* **47**, 1799–1813.

Oort, A.H., and J. J. Yienger, 1996: Observed interannual variability in the Hadley circulation and its connection to ENSO. *J. Climate*, **9**, 2751-2767.

PCMDI 2005a: http://www-pcmdi.llnl.gov/ipcc/model_documentation/GFDL-cm2.htm

PCMDI 2005b: http://www-pcmdi.llnl.gov/ipcc/model_documentation/GISS-E.htm

PCMDI 2005c: http://www-pcmdi.llnl.gov/ipcc/model_documentation/CCSM3.htm

PCMDI 2005d: http://www-pcmdi.llnl.gov/ipcc/model_documentation/PCM.htm

PCMDI 2005e: http://www-pcmdi.llnl.gov/ipcc/model_documentation/MIROC3.2_hires.htm

Rayner, N.A., D. E. Parker, E. B. Horton, C. K. Folland, L.V. Alexander, D. P. Rowell, E.C. Kent, and A. Kaplan, 2003: Globally complete analyses of sea surface temperature, sea ice and night marine air temperature. maximum temperature gradients (September-October) in the tropical Pacific. *J. Geophys. Rev.*, **108**, 1871-2000.

Rasmusson, E. M., and T. H. Carpenter, 1982: Variations in tropical sea surface temperature and surface wind fields associated with the southern oscillation/ El Niño. *Mon. Wea. Rev.*, **110**, 354-384.

Ropelewski, C.F., and M.S. Halpert, 1987: Global and regional scale precipitation patterns

- associated with the El Niño/Southern oscillation. *Mon. Wea. Rev.*, **115**, 1606-1626.
- Thompson C. J., and D. Battisti, 2001: A linear dynamical model of ENSO. Part II: Analysis. *J. Climate*, **14**, 445-466.
- Timmermann, A., J. Oberhuber, A. Bacher, M. Esch, M. Latif and E. Roeckner, 1999: Increased El Niño frequency in a climate model forced by future greenhouse warming. *Nature*, **398**, 694-696.
- Torrence, C., and P. Webster, 1998: The annual cycle of persistence in the El Niño Southern oscillation. *Quart. J. Roy. Meteor. Soc.*, **124**, 1985-2004.
- Trenberth, K.E., 1997: The definition of El Niño. *Bull. Amer. Meteor. Soc.*, **78**, 2771-2777.
- Trenberth K.E., and D. P. Stepaniak, 2001: Indices of El Niño evolution. *J. Climate*, **14**, 1697-1701.
- Trenberth K.E., G.W. Branstator, Karoly D., Kumar A., Lau N.C., Ropelewski C., 1998: Progress during TOGA in understanding and modeling global teleconnections associated with tropical sea surface temperatures. *J. Geophys. Res.*, **103**, 14291-14324.
- van Oldenborgh G.J, S. Philip, and M. Collins, 2005: El Niño in a changing climate: a multi -model study. (Submitted to *Ocean Sci.*)
- Wallace, J. M., and D. S. Gutzler, 1981: Teleconnections in the geopotential height field during the Northern Hemisphere winter. *Mon. Wea. Rev.*, **109**, 784–812.
- Wang, B., 1995: Interdecadal changes in El Niño onset in the last four decades. *J. Climate*, **8**, 267-284.
- Wittenberg, A. T., A. Rosati, N.-C. Lau, and J. J. Ploshay, 2005: GFDL's CM2 global coupled climate models, Part 3: Tropical Pacific climate and ENSO. *J. Climate*, in press.
- Xie P., and P. A. Arkin, 1997: Global Precipitation: A 17-year monthly analysis based on gauge observations, satellite estimates, and numerical model outputs, *Bull. Amer. Meteor. Soc.*, **78**, 2539-2558.

FIGURE CAPTIONS

Figure 1: Nino3 SST index regressions on observed and simulated SSTs in the 1950-1999 period; based on all calendar month anomalies. The marked rectangular box outlines the Nino3 region (5°S-5°N;150°W-90°W). SST observations are from the HadISST analysis. Simulating models are noted at the left of each panel. Contour interval is 0.2K and the zero contour is suppressed; shading threshold is 0.6K.

Figure 2: Autocorrelation of Nino3 SST indices, over an 18-month lead/lag period. Horizontal lines are drawn at $e^{-1}=0.368$ and 0.0 to facilitate estimation of the ENSO life-cycle.

Figure 3: ENSO SST evolution at the equator (5°S-5°N), obtained from lead/lag regressions of the Nino3 SST index over a 42-month period. Top panels show observed SST evolution in the full record (top-left), pre-climate-transition period (1950-1976, top-middle), and post-transition period (1977-1999, top-right). All six model regressions are from the full 50-year period. Contour interval is 0.2K and the zero contour is suppressed; shading threshold is 0.2K. Note, time markings have no unique correspondence with calendar months.

Figure 4: Seasonal phase-locking of ENSO variability: Standard deviation of the Nino3.4 SST index is shown in each calendar month. Note, the GFDL values have been scaled down by a factor of 2 before display.

Figure 5: ENSO winter teleconnections to tropical precipitation and extratropical circulation: Nino3 SST index regressions on tropical precipitation are shown in the left panels, using a contour interval and shading threshold of 0.4 mm/day. 250 hPa geopotential height regressions are shown in polar plots in the right panels, with contour interval and shading threshold of 10m; zero contour is suppressed in both cases. Regressions are on monthly December-March data. Simulation targets – regressions on global reanalyses – are shown in the top-two panels; period is 1950-1999 for NCEP and 1958-2000 for ERA-40. Six pairs of model regressions follow (contd. on next page). The core ENSO rainfall region (180°-150°W, 7.5°S-5°N) over which vertical velocity profiles are examined in figure 6 is shown in the ERA-40 panel using a red rectangle.

Figure 6: ENSO vertical velocity ($-\omega$) profiles: Nino3 regressions on pressure vertical velocity are averaged over the core rainfall region in the central equatorial Pacific (180°-150°W, 7.5°S-5°N). The averaging region is shown using a red rectangle on the ERA-40 precipitation panel in figure 5.

Figure 7: ENSO winter teleconnections to North American hydroclimate: Nino3 SST index regressions on Pacific / North American precipitation are shown in the left panels, using a contour interval of 0.1 mm/day for values greater than 0.2 mm/day. Surface air temperature regressions are shown in right panels, with contour interval and shading threshold of 0.2K; zero contour is suppressed in both cases. Regressions are on monthly December-March data. Simulation targets – regressions on global reanalyses – are shown in the top-two panels; period is 1950-1999 for NCEP and 1958-2000 for ERA-40. Six pairs of model regressions follow (contd. on next page).

Figure 8: ENSO's zonally-symmetric winter circulation response in the Tropics/Subtropics: Nino3 SST index regressions on zonal-mean zonal wind (rotational flow) are shown using contour interval and shading threshold of 0.5 m/s; zero contour is omitted in all panels. Regressions on divergent (Hadley) circulation are shown using vectors, whose zonal component denotes zonal-mean meridional wind (in m/s); and vertical component, the zonal-mean vertical velocity (in Pa/hour). Vectors of magnitude less than 0.05 are suppressed. The same vector scale, shown below the panels, is used in all cases.

Nino3 SST Regressions

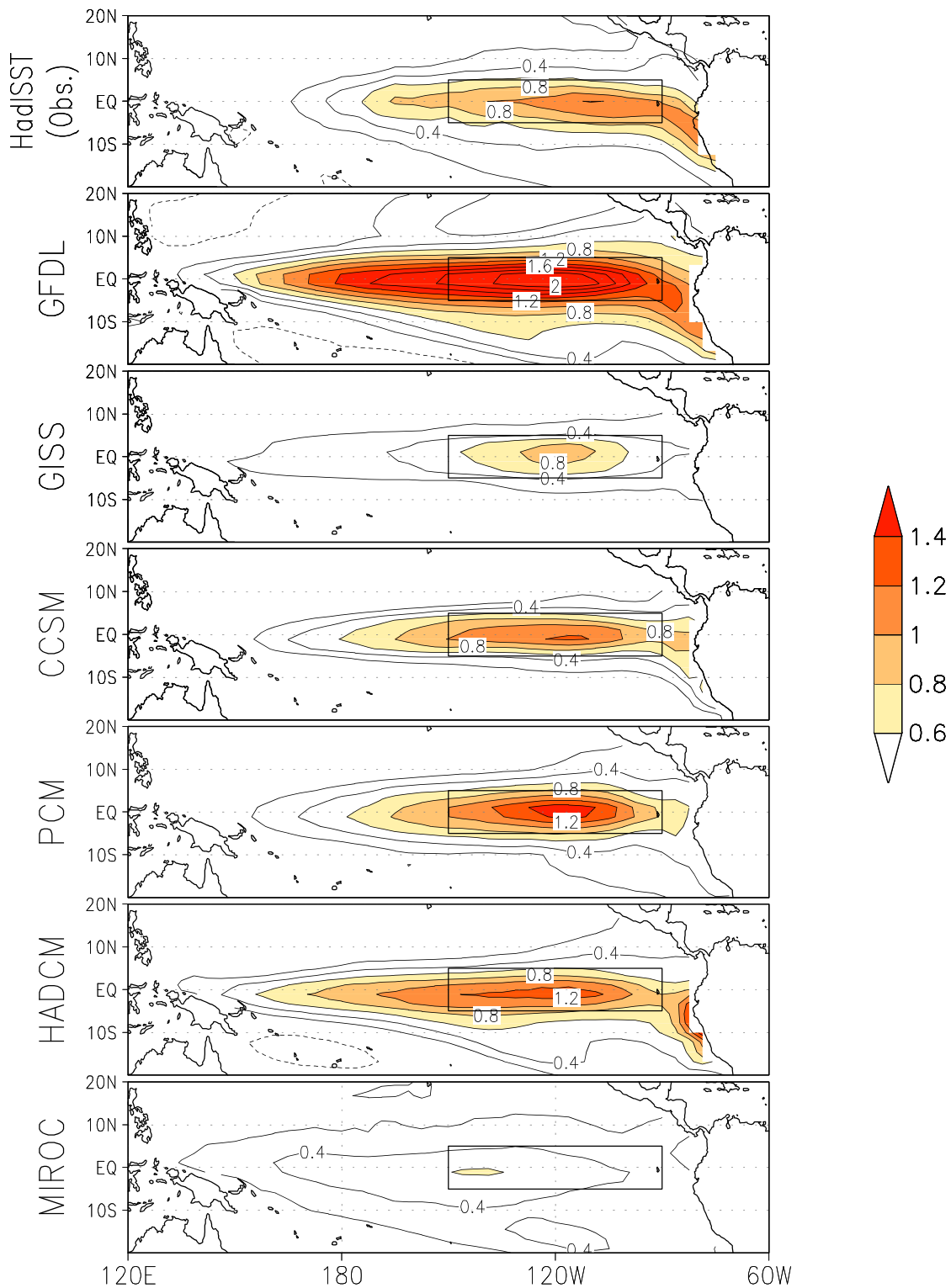


Figure 1: Nino3 SST index regressions on observed and simulated SSTs in the 1950-1999 period; based on all calendar month anomalies. The marked rectangular box outlines the Nino3 region (5°S-5°N;150°W-90°W). SST observations are from the HadISST analysis. Simulating models are noted at the left of each panel. Contour interval is 0.2K and the zero contour is suppressed; shading threshold is 0.6K.

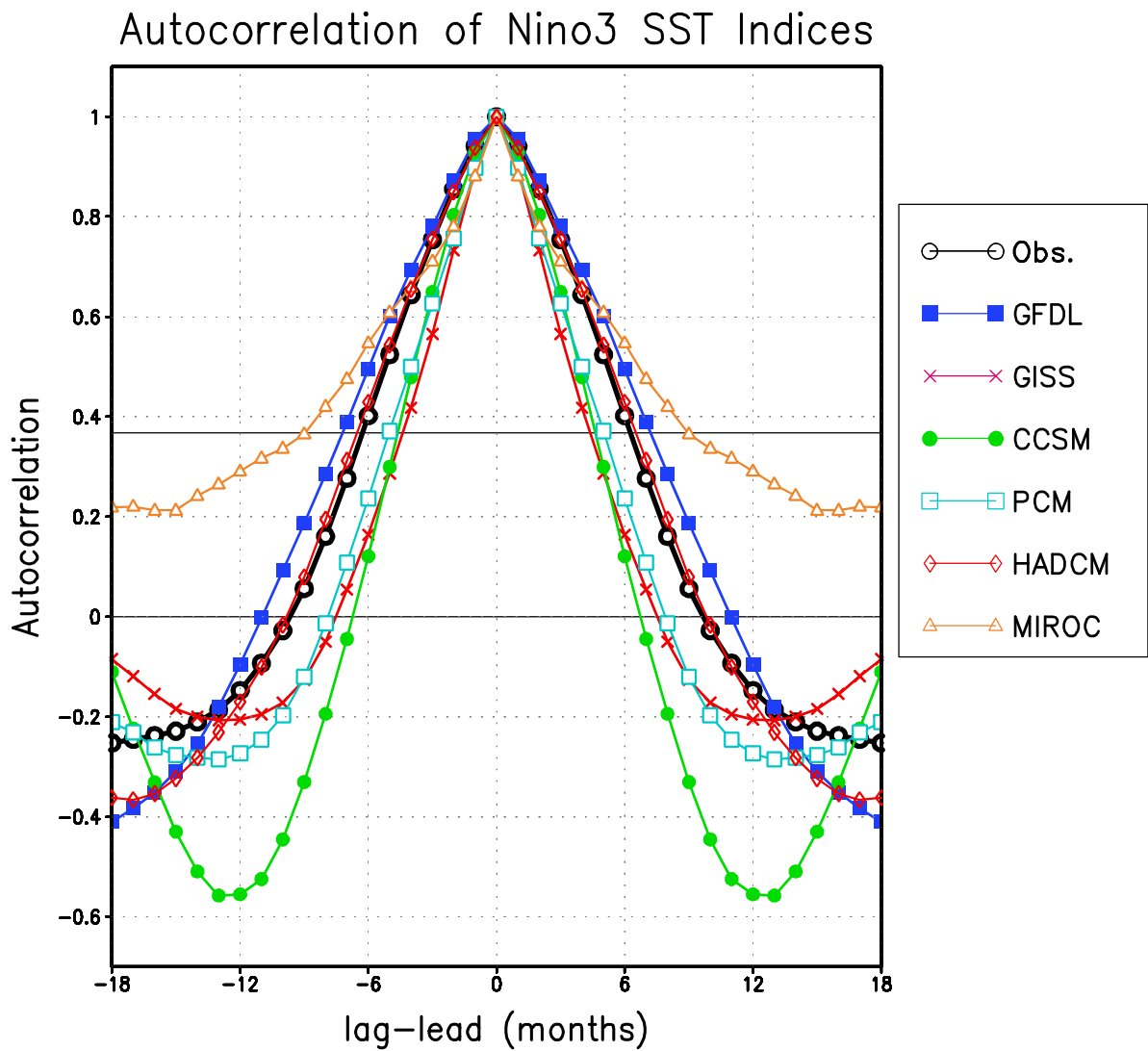


Figure 2: Autocorrelation of Nino3 SST indices, over an 18-month lead/lag period. Horizontal lines are drawn at $e^{-1}=0.368$ and 0.0 to facilitate estimation of the ENSO life-cycle.

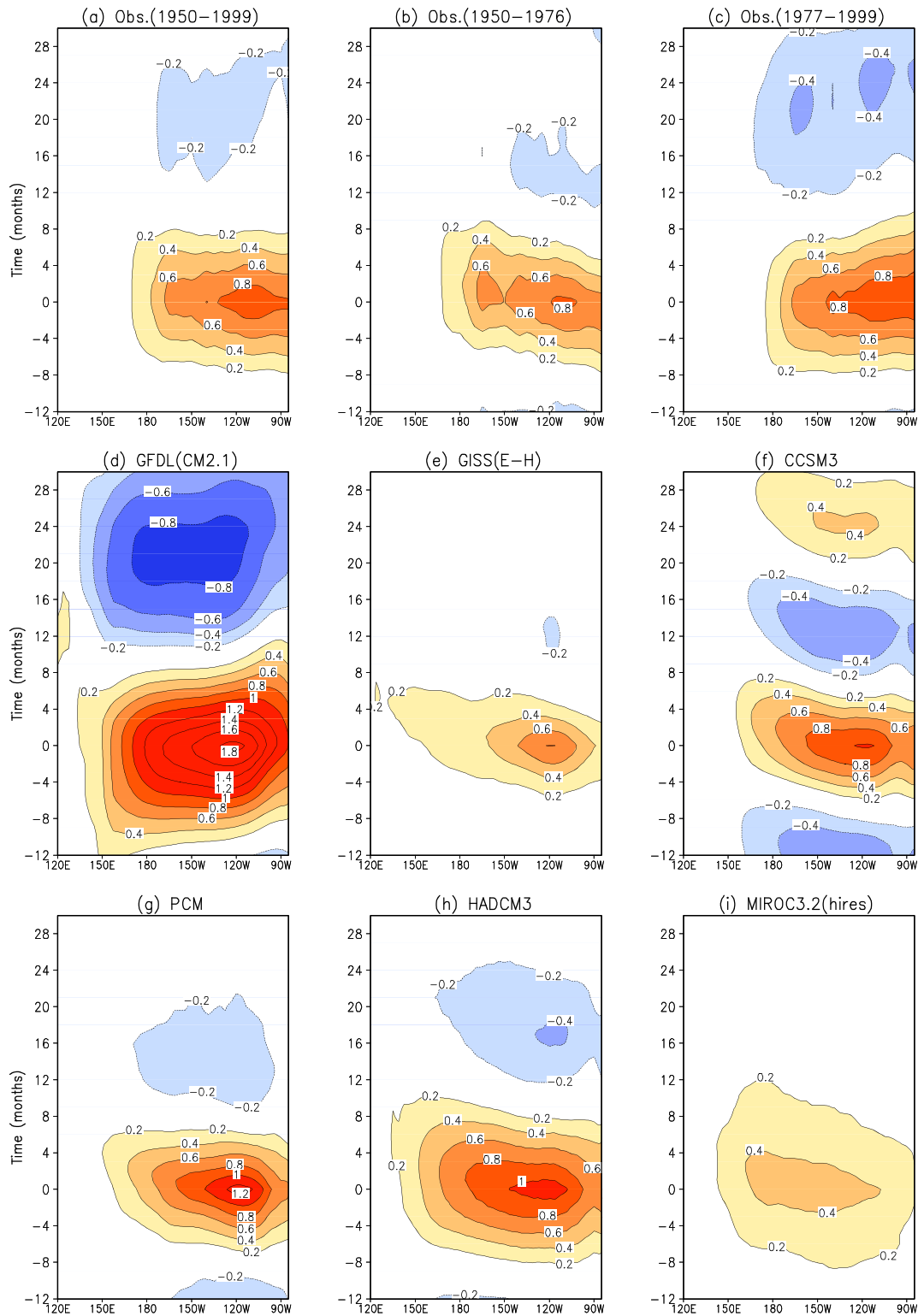


Figure 3: ENSO SST evolution at the equator (5°S - 5°N), obtained from lead/lag regressions of the Niño3 SST index over a 42-month period. Top panels show observed SST evolution in the full record (top-left), pre-climate-transition period (1950-1976, top-middle), and post-transition period (1977-1999, top-right). All six model regressions are from the full 50-year period. Contour interval is 0.2K and the zero contour is suppressed; shading threshold is 0.2K. Note, time markings have no unique correspondence with calendar months.

Phase Locking of ENSO

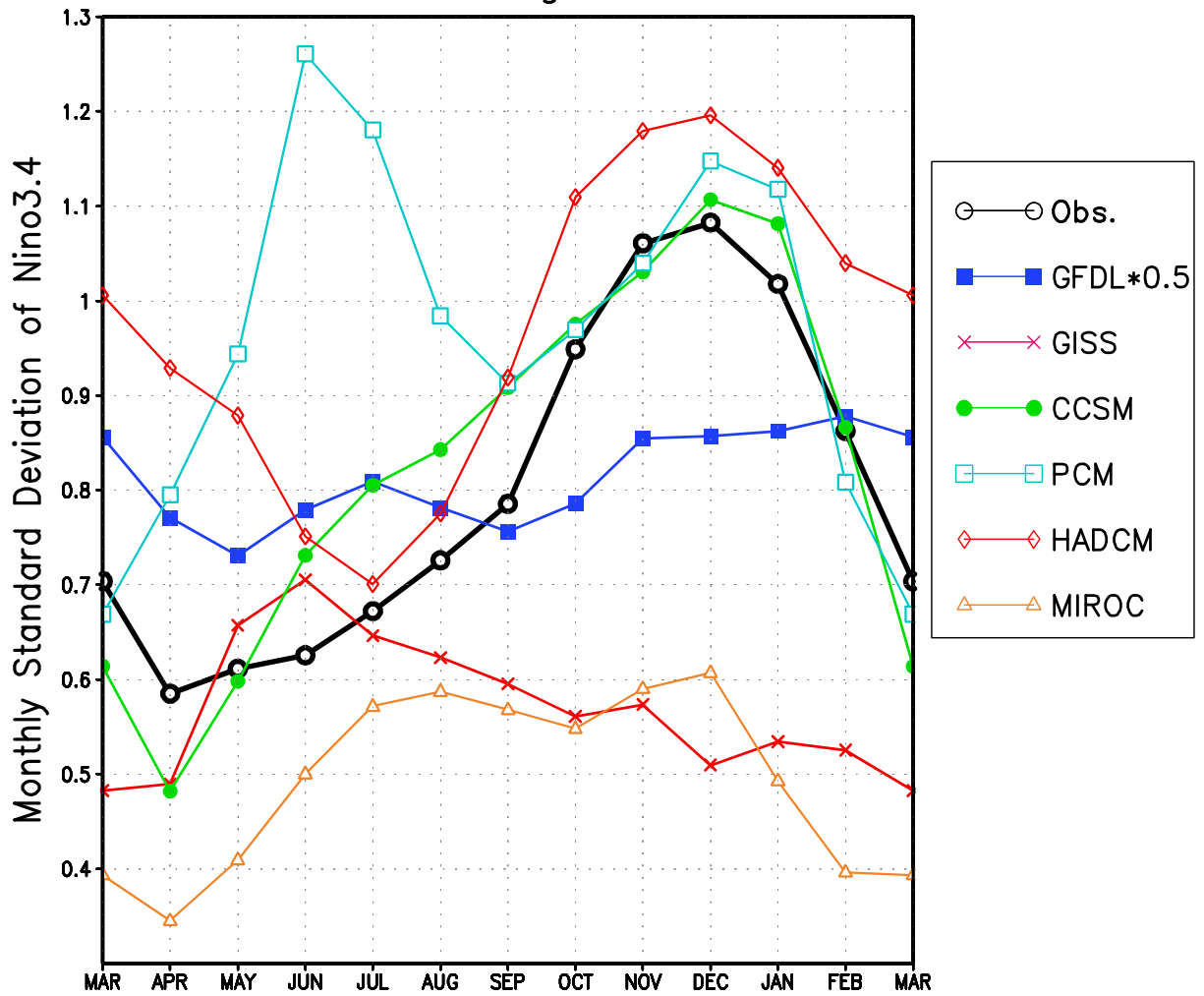


Figure 4: Seasonal phase-locking of ENSO variability: Standard deviation of the Nino3.4 SST index is shown in each calendar month. Note, the GFDL values have been scaled down by a factor of 2 before display.

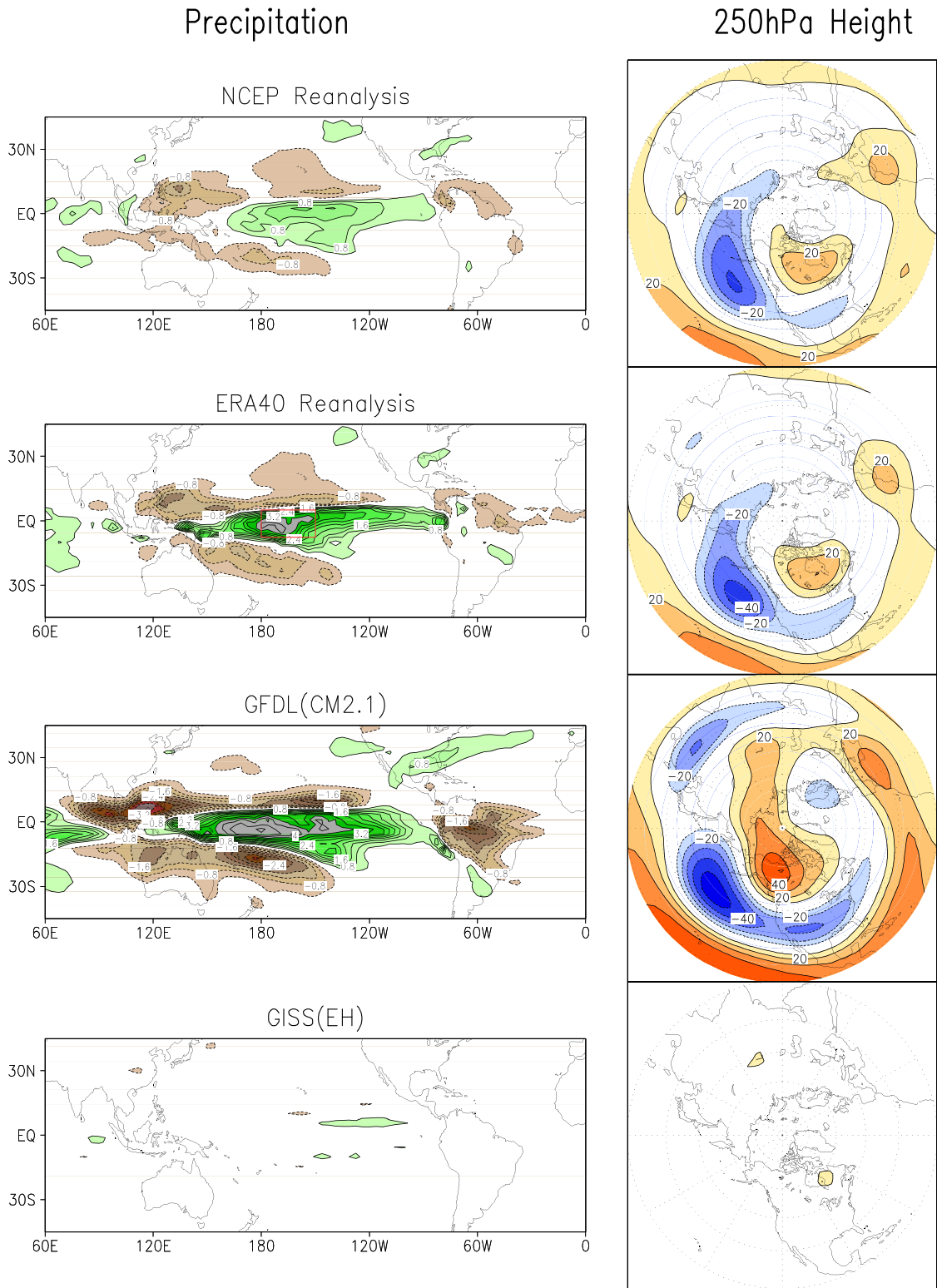


Figure 5: ENSO winter teleconnections to tropical precipitation and extratropical circulation: Nino3 SST index regressions on tropical precipitation are shown in the left panels, using a contour interval and shading threshold of 0.4 mm/day. 250 hPa geopotential height regressions are shown in polar plots in the right panels, with contour interval and shading threshold of 10m; zero contour is suppressed in both cases. Regressions are on monthly December-March data. Simulation targets – regressions on global reanalyses – are shown in the top-two panels; period is 1950-1999 for NCEP and 1958-2000 for ERA-40. Six pairs of model regressions follow (contd. on next page). The core ENSO rainfall region (180°-150°W, 7.5°S-5°N) over which vertical velocity profiles are examined in figure 6 is shown in the ERA-40 panel using a red rectangle.

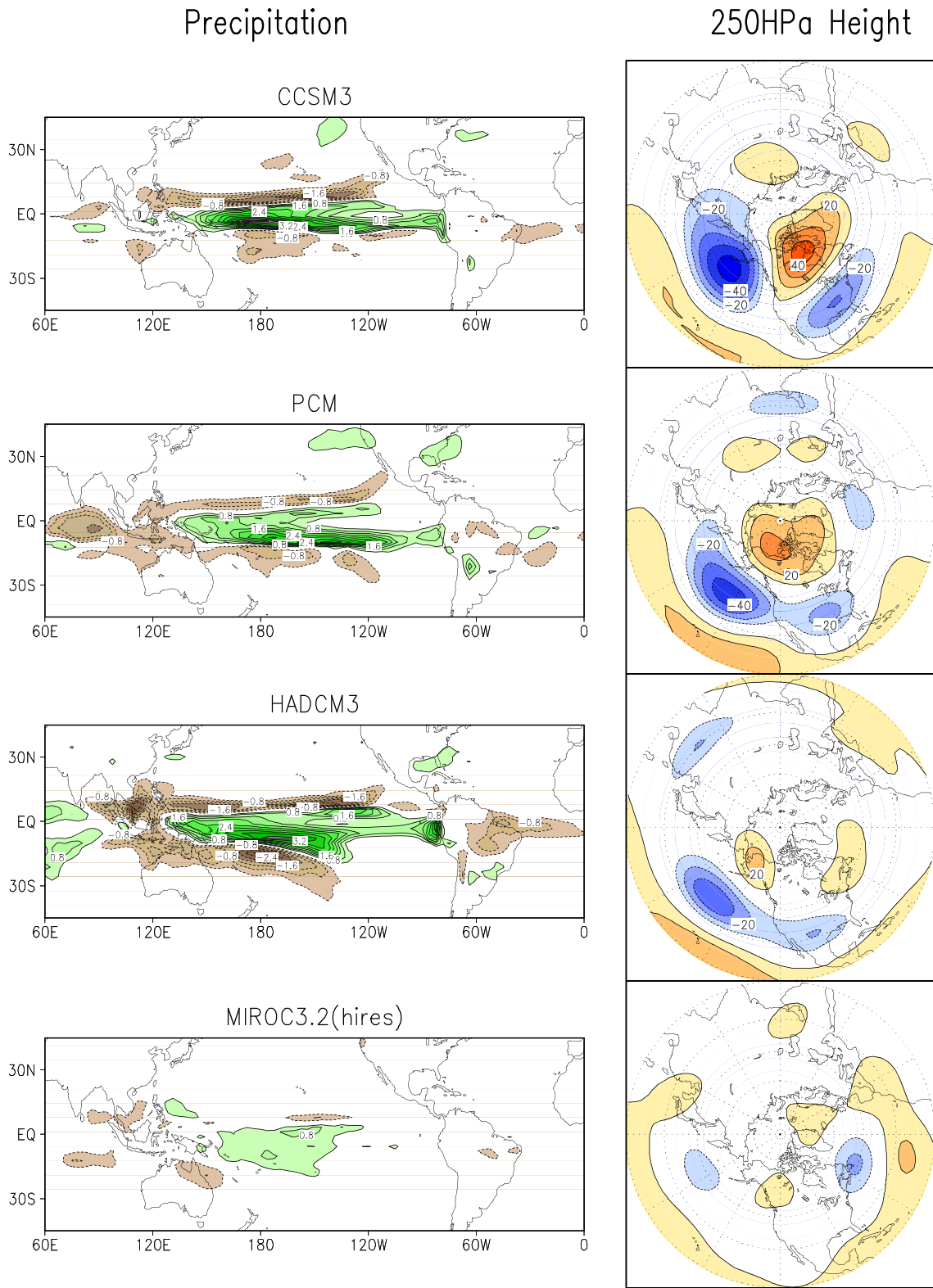


Figure 5 (contd.): ENSO winter teleconnections to tropical precipitation and extratropical circulation:

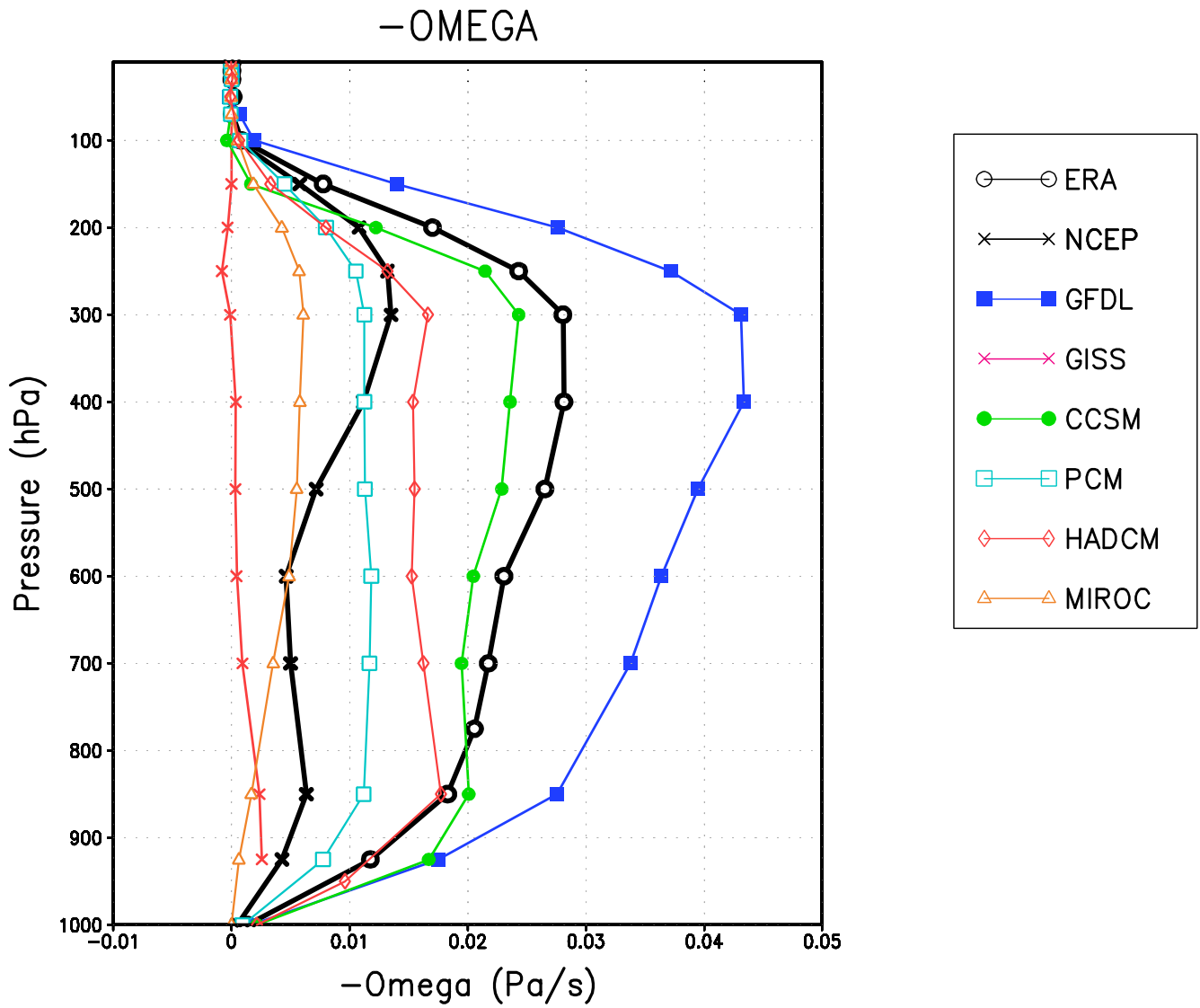
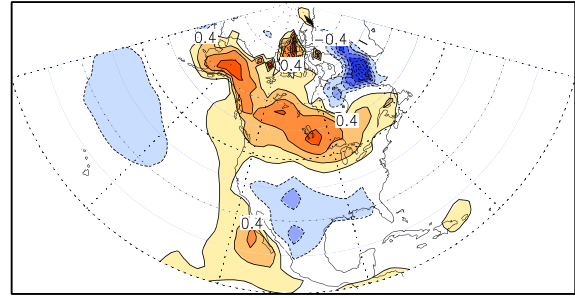
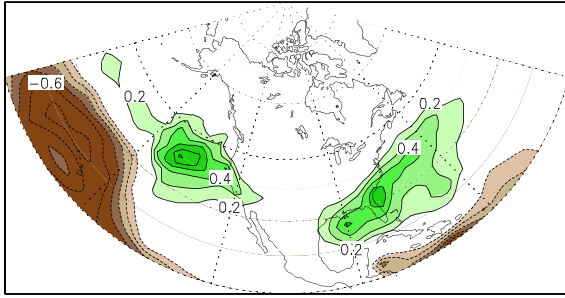


Figure 6: ENSO vertical velocity ($-\omega$) profiles: Nino3 regressions on pressure vertical velocity are averaged over the core rainfall region in the central equatorial Pacific (180° - 150° W, 7.5° S- 5° N). The averaging region is shown using a red rectangle on the ERA-40 precipitation panel in figure 5.

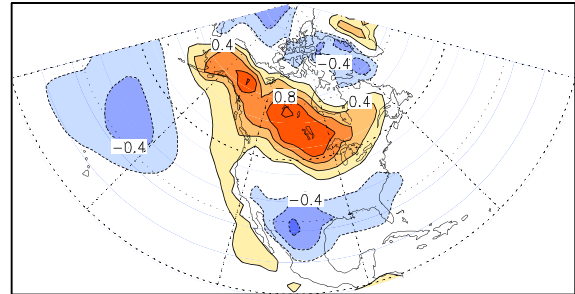
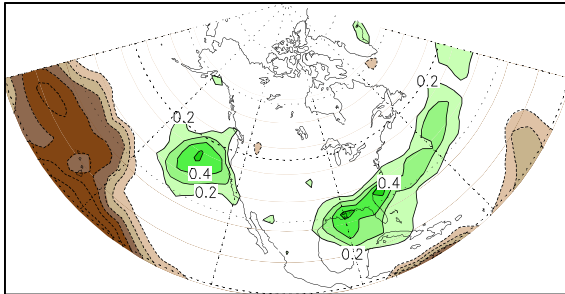
Precipitation

Surface Temperature

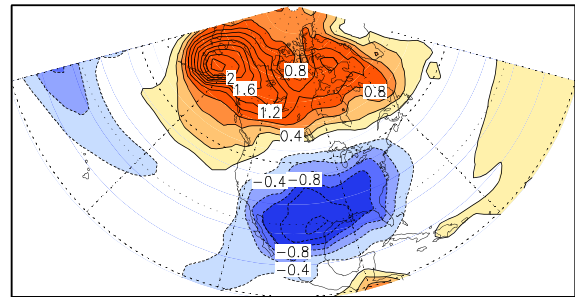
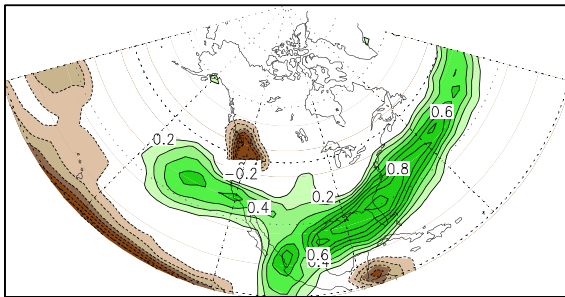
NCEP Reanalysis



ERA40 Reanalysis



GFDL CM2.1



GISS-EH

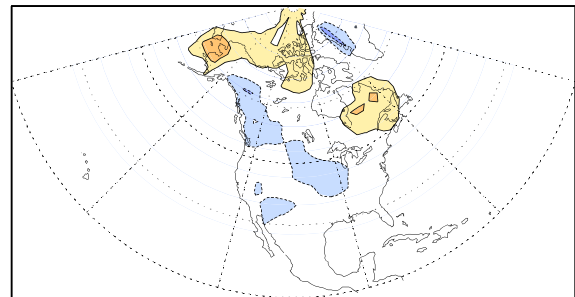
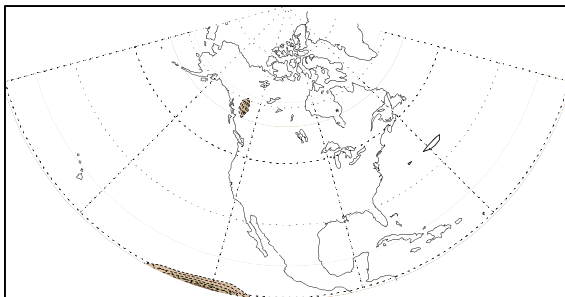
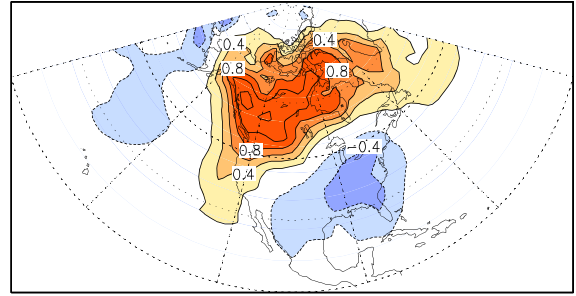
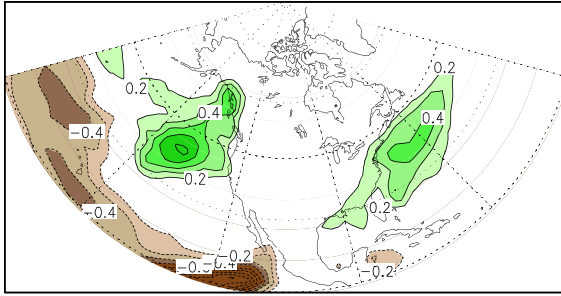


Figure 7: ENSO winter teleconnections to North American hydroclimate: Nino3 SST index regressions on Pacific / North American precipitation are shown in the left panels, using a contour interval of 0.1 mm/day for values greater than 0.2 mm/day. Surface air temperature regressions are shown in right panels, with contour interval and shading threshold of 0.2K; zero contour is suppressed in both cases. Regressions are on monthly December-March data. Simulation targets – regressions on global reanalyses – are shown in the top-two panels; period is 1950-1999 for NCEP and 1958-2000 for ERA-40. Six pairs of model regressions follow (contd. on next page).

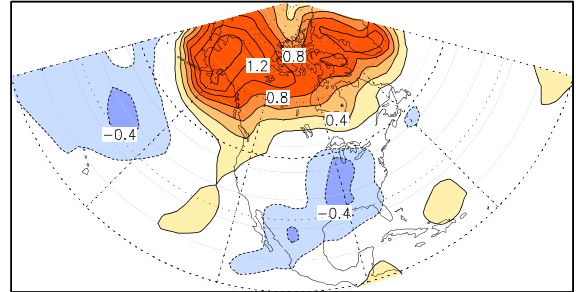
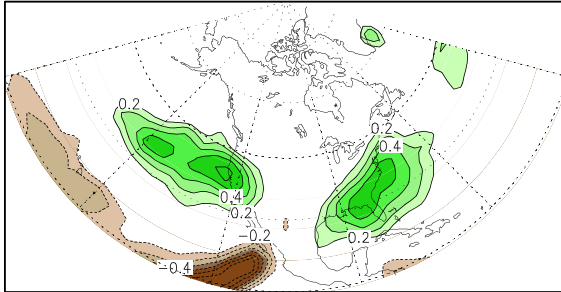
Precipitation

Surface Temperature

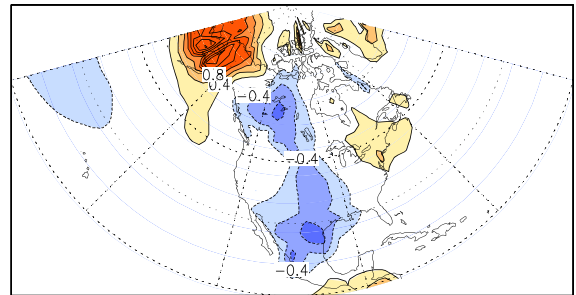
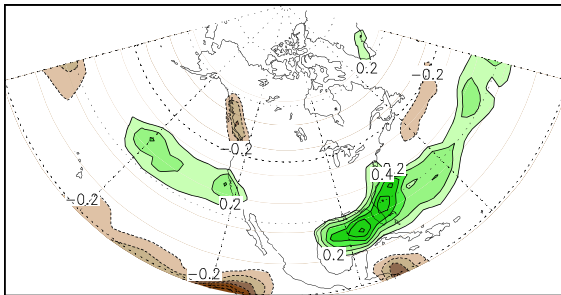
CCSM3



PCM



HADCM3



MIROC3.2(hires)

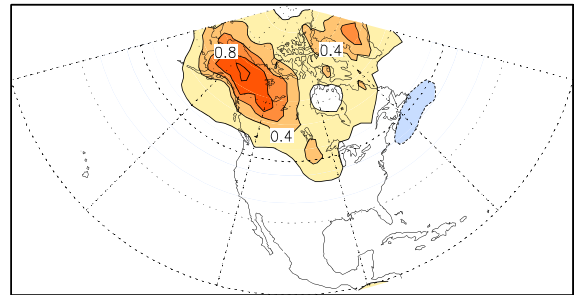
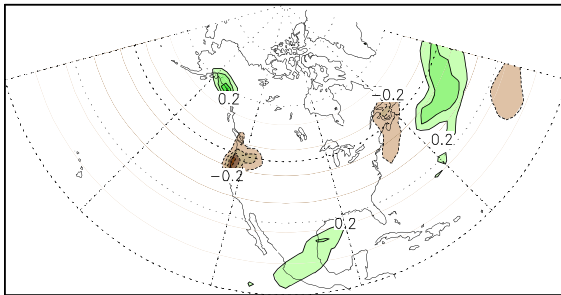


Figure 7 (contd.): ENSO winter teleconnections to North American hydroclimate:

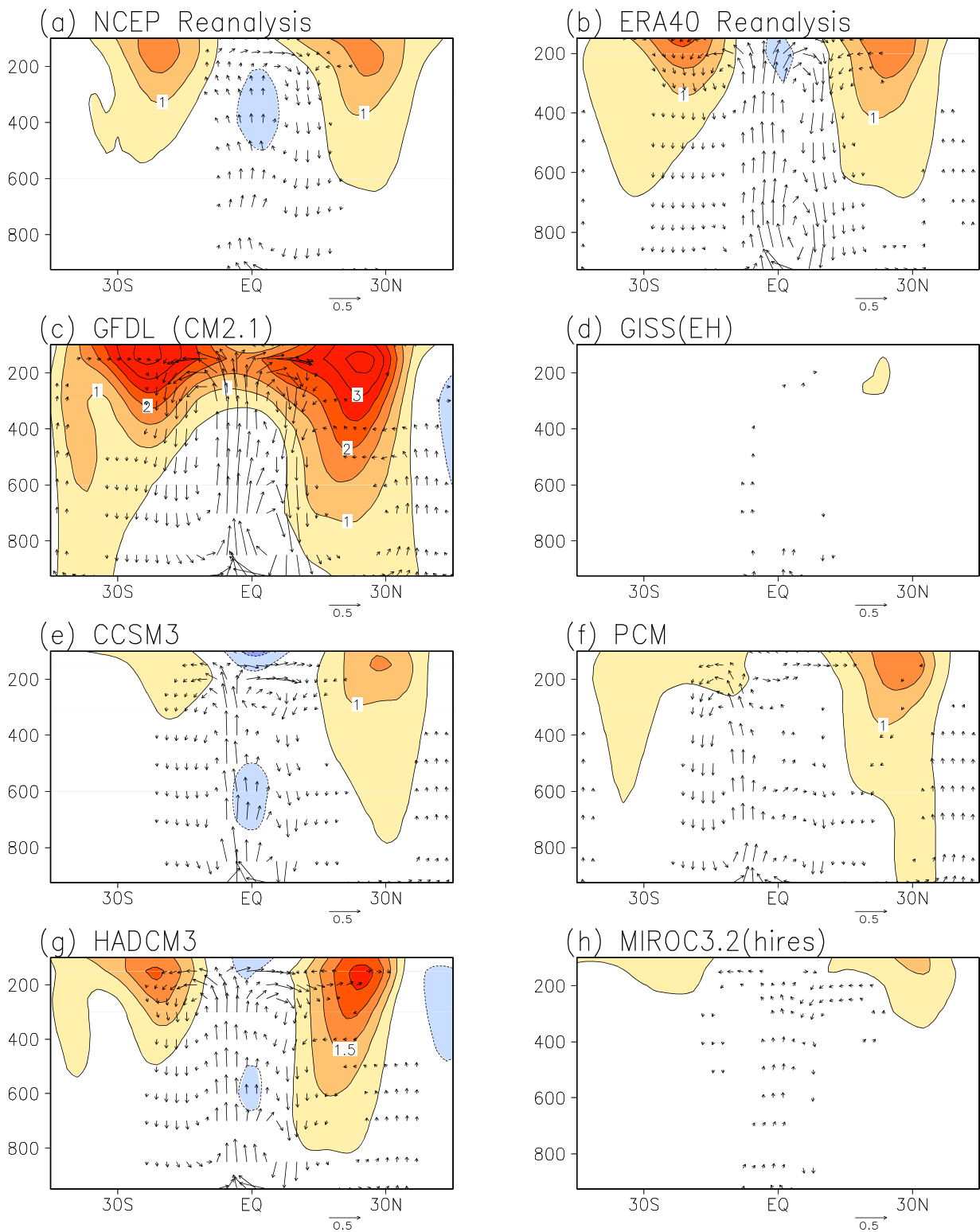


Figure 8: ENSO's zonally-symmetric winter circulation response in the Tropics/Subtropics: Nino3 SST index regressions on zonal-mean zonal wind (rotational flow) are shown using contour interval and shading threshold of 0.5 m/s; zero contour is omitted in all panels. Regressions on divergent (Hadley) circulation are shown using vectors, whose zonal component denotes zonal-mean meridional wind (in m/s); and vertical component, the zonal-mean vertical velocity (in Pa/hour). Vectors of magnitude less than 0.05 are suppressed. The same vector scale, shown below the panels, is used in all cases.